

Kinematics and H₂ morphology of the multipolar post-AGB star IRAS 16594–4656[★]

G. C. Van de Steene¹, T. Ueta^{1,2}, P. A. M. van Hoof¹, M. Reyniers³, and A. G. Ginsburg⁴

¹ Royal Observatory of Belgium, Ringlaan 3, 1180 Brussels, Belgium
e-mail: [gsteene;pvh@oma.be]

² Department of Physics and Astronomy, University of Denver, 2112 E. Wesley, Denver, CO 80208, USA
e-mail: tueta@du.edu

³ Instituut voor Sterrenkunde, KU Leuven, Celestijnenlaan 200D, 3001 Leuven, Belgium
e-mail: maarten@ster.kuleuven.ac.be

⁴ Department of Astrophysical and Planetary Sciences, University of Colorado, Boulder, CO 80309, USA

Received 19 October 2007 / Accepted 21 December 2007

ABSTRACT

Context. The spectrum of IRAS 16594–4656 shows shock-excited H₂ emission and collisionally excited emission lines such as [O I], [C I], and [Fe II].

Aims. The goal is to determine the location of the H₂ and [Fe II] shock emission, to determine the shock velocities, and to constrain the physical properties in the shock.

Methods. High resolution spectra of the H₂ 1–0 S(1), H₂ 2–1 S(1), [Fe II], and Pa β emission lines were obtained with the near infrared spectrograph Phoenix on Gemini South.

Results. The position-velocity diagrams of H₂ 1–0 S(1), H₂ 2–1 S(1), and [Fe II] are presented. The H₂ and [Fe II] emission is spatially extended. The collisionally excited [O I] and [C I] optical emission lines have a similar double-peaked profile compared to the extracted H₂ profile and appear to be produced in the same shock. They all indicate an expansion velocity of ~ 8 km s⁻¹ and the presence of a neutral, very high-density region with n_e about 3×10^6 to 5×10^7 cm⁻³. However, the [Fe II] emission is single-peaked. It has a Gaussian *FWHM* of 30 km s⁻¹ and a total width of 62 km s⁻¹ at 1% of the peak. The Pa β profile is even wider with a Gaussian *FWHM* of 48 km s⁻¹ and a total width of 75 km s⁻¹ at 1% of the peak.

Conclusions. The H₂ emission is excited in a slow 5 to 20 km s⁻¹ shock into dense material at the edge of the lobes, caused by the interaction of the AGB ejecta and the post-AGB wind. The 3D representation of the H₂ data shows a hollow structure with less H₂ emission in the equatorial region. The [Fe II] emission is not present in the lobes, but originates close to the central star in fast shocks in the post-AGB wind or in a disk. The Pa β emission also appears to originate close to the star.

Key words. shock waves – stars: AGB and post-AGB – stars: winds, outflows – stars: individual : IRAS 16594–4656 – ISM: molecules

1. Introduction

Post-asymptotic giant branch (AGB) stars represent an important transition phase in the evolution of low and intermediate-mass stars, between the AGB and the planetary nebula (PN) phases. During this period, the detached circumstellar envelope of gas and dust is expanding away from the star. Meanwhile the star itself is increasing in temperature at nearly constant luminosity. This phase lasts a few hundred to a few thousand years depending upon the star's core mass. When the temperature is high enough and the star photoionizes the nebula, it has entered the PN phase (e.g. Kwok 1993). In spite of extensive study, the evolution from the AGB toward the PN stage is still poorly understood. The drastic changes observed in circumstellar structure and kinematics are particularly puzzling. During the late AGB or early post-AGB evolutionary stages, the geometry of the circumstellar material changes from more or less spherically symmetric to axially symmetric, with the result that most PNe

exhibit axisymmetric structures, ranging from elliptical to bipolar (e.g., Balick & Frank 2002).

Bipolar PNe frequently possess molecular envelopes that are readily detectable in the near-infrared ro-vibrational lines of H₂ (Kastner et al. 1996; Kelly & Hrivnak 2005). The available data suggest that the onset of near-infrared H₂ emission in PNe can be traced back to the proto-planetary nebula (PPN) phase but not back to the AGB phase of evolution (Weintraub et al. 1998; Davis et al. 2005). These observations suggest that further studies of H₂ emission from PPNe may offer insight into the transition from AGB star to PN and from spherical to axisymmetric mass loss. The study of transition objects showing H₂ emission at an early stage is crucial for understanding the hydrodynamic processes shaping the nebulae. The H₂ lines can reveal details about the physical conditions in the shocks associated with these hydrodynamic processes and thereby help constrain models of the interaction of the central star with the AGB remnant.

IRAS 16594–4656 is classified as a post-AGB star for several reasons. In the IRAS color-color diagram it has the colors of a PN (Van de Steene & Pottasch 1993), but it has not been detected in the radio continuum at 3 or 6 cm. It has a large infrared excess due to dust with a color temperature of 173 K.

[★] Based on observations collected at the Gemini-South with the Phoenix instrument under GS-2003A-Q-41, and VLT under 65.L-0615(A).

It displays a double-peaked spectral energy distribution, with the peak in the mid-infrared much brighter than the peak in the near-infrared (Van de Steene et al. 2000a). It possesses a CO envelope with an expansion velocity of 14 km s^{-1} (Woods et al. 2005). The chemistry of IRAS 16594–4656 appears to be carbon-rich. This is based on the detection of unidentified IR emission features at 3.3 , 6.2 , 7.7 , 8.6 , 11.3 , 12.6 , and $13.4 \mu\text{m}$, as well as the $21 \mu\text{m}$ feature (García-Lario et al. 1999), all commonly associated with a carbon-rich chemistry. The optical spectrum of IRAS 16594–4656 shows a spectral type B7 with significant reddening. The H α emission has a P-Cygni type profile indicative of a stellar wind (Van de Steene et al. 2000b). In Van de Steene & van Hoof (2003, hereafter Paper I) we derived the total extinction value (i.e., interstellar and circumstellar extinction combined) using the extinction law of Cardelli et al. (1989). We found $A_V = 7.5 \pm 0.4 \text{ mag}$ with $R_V = 4$. With this extinction value and the flux calibration from the Kurucz model, we determined a distance of $(2.2 \pm 0.4) L_4^{1/2} \text{ kpc}$, which was in good agreement with the distance of $2.5 L_4^{1/2} \text{ kpc}$ derived by Su et al. (2001) (with L_4 the luminosity in units of $10^4 L_\odot$).

In the optical the nebulosity is dominated by scattered light. HST WFPC2 images showed that the object is a multipolar reflection nebula with 3 extensions on each side (e.g., Hrivnak et al. 1999). It has been interpreted as a bipolar outflow episodically channeled from a rotating/precessing torus. The outer nebula also shows concentric arcs (Hrivnak et al. 2001). High resolution mid-infrared images in the N and Q-band show a bright equatorial torus viewed almost edge-on and a pair of bipolar lobes, which show a close correspondence with the H₂ HST map. The shape of the bipolar lobes shows that the fast outflow is still confined by the remnant AGB shell (Volk et al. 2006). The elongation of the inner nebula is along the symmetry axis of this torus at $\sim 80^\circ$ PA, and it seems likely that the material ejection is channeled into the bipolar lobes by the torus and/or some other collimation mechanism (García-Hernández et al. 2004). Ueta et al. (2005, 2007) found, based on polarized-flux images, that the inner structure of the nebula is clearly elongated in the east-west direction ($5''.0 \times 2''.0$ at PA 81°). Their polarized flux maps uncover the bipolar cusp structure of the shell, corresponding to the main elongation in intensity, and a hollow shell structure which delineates the wall of the elongated bipolar cavities.

In Paper I we examined the near-infrared spectrum of IRAS 16594–4656. It shows strong H₂ emission lines and some typical metastable shock-excited lines such as [Fe II] 1.257 & $1.644 \mu\text{m}$. We argued that the molecular hydrogen emission is mainly collisionally excited in a C-type shock. However, H₂ and [Fe II] emission don't usually coexist. The goal of this paper is to clarify the location of the H₂ and [Fe II] shock emission in this object and to determine the shock velocities.

High resolution near-infrared spectra of IRAS 16594–4656 have been obtained with the near infrared high resolution spectrograph Phoenix on Gemini South. The observations and data reduction are discussed in Sect. 2. The results of the analysis are presented in Sect. 3, and the morphology, kinematics, and shock properties are discussed in Sect. 4, and finally we present some conclusions in Sect. 5.

2. Observations and data reduction

2.1. High resolution infrared spectra

The spectra were obtained in service mode with the near infrared high resolution spectrograph Phoenix (Hinkle et al. 2002) on

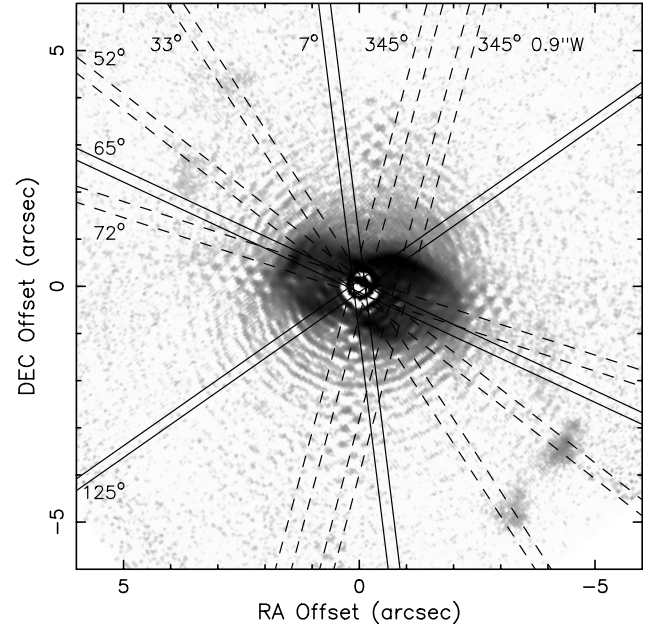


Fig. 1. HST/NICMOS H₂ 1–0 S(1) image (north is up and east to the left) showing the slit positions. The slit positions displayed are at 7° , 65° , and 125° PA with $0''.25$ width (this work; solid line) and at 33° , 52° , 72° , 345° PA, and 345° PA offset $0''.9$ west of the star with $0''.34$ width (Hrivnak et al. 2006; dashed line).

Gemini South at 3 position angles (PA), through regions showing bright H₂ emission : at 7° , 65° , and 125° . The position angle is measured in degrees east of north. The slit positions are shown on top of the HST H₂ 1–0 S(1) image in Fig. 1. The slit length is $14''$ and slit width is 3 pixels or $0''.25$, giving a resolution of $\sim 60\,000$. On 5 May 2003 the integration times were $4 \times 300 \text{ s}$ for H₂ 1–0 S(1) $2.12125 \mu\text{m}$ through filter K4748/4712.82 and $4 \times 200 \text{ s}$ for [Fe II] $1.64355 \mu\text{m}$ through filter H6073/6082.93 at each position angle. H₂ 2–1 S(1) $2.2471 \mu\text{m}$ was observed for $4 \times 300 \text{ s}$ at each position angle through filter K4484/4448.98 on 1 August 2003. Next, in the same night, Pa β was observed, however the weather conditions were quickly deteriorating and we obtained only one useful image of Pa β before the dome had to be closed.

In the archive there was another set of H₂ 1–0 S(1) data available for this object taken with Phoenix under GS-2003A-Q-27 (PI: B. J. Hrivnak; Hrivnak et al. 2006) at 33° , 52° , 72° , 345° PA through the star, and at 345° PA offset $0''.9$ west of the star, all with a slit width of $0''.35$ giving a resolution of $\sim 50\,000$. We include this data set in our analysis for the sake of completeness and in order to reconstruct the 3-dimensional structure of the H₂ shell.

Basic data reduction (such as flatfielding and sky subtraction) was done in IRAF using the scripts provided by the Phoenix team. Next the images were rectified by fitting the position of the continuum peak in the spatial dimension along all pixels in the spectral dimension. Then the images were combined to generate cross-correlated, co-added images. Continuum emission was subtracted from the data by fitting the emission of the source in the spectral dimension before co-adding. The wavelength calibration was done using telluric lines in the standard star spectrum using the HITRAN 2000 database (Rothman et al. 2003). The resulting position-velocity diagrams are presented in Figs. 2–4.

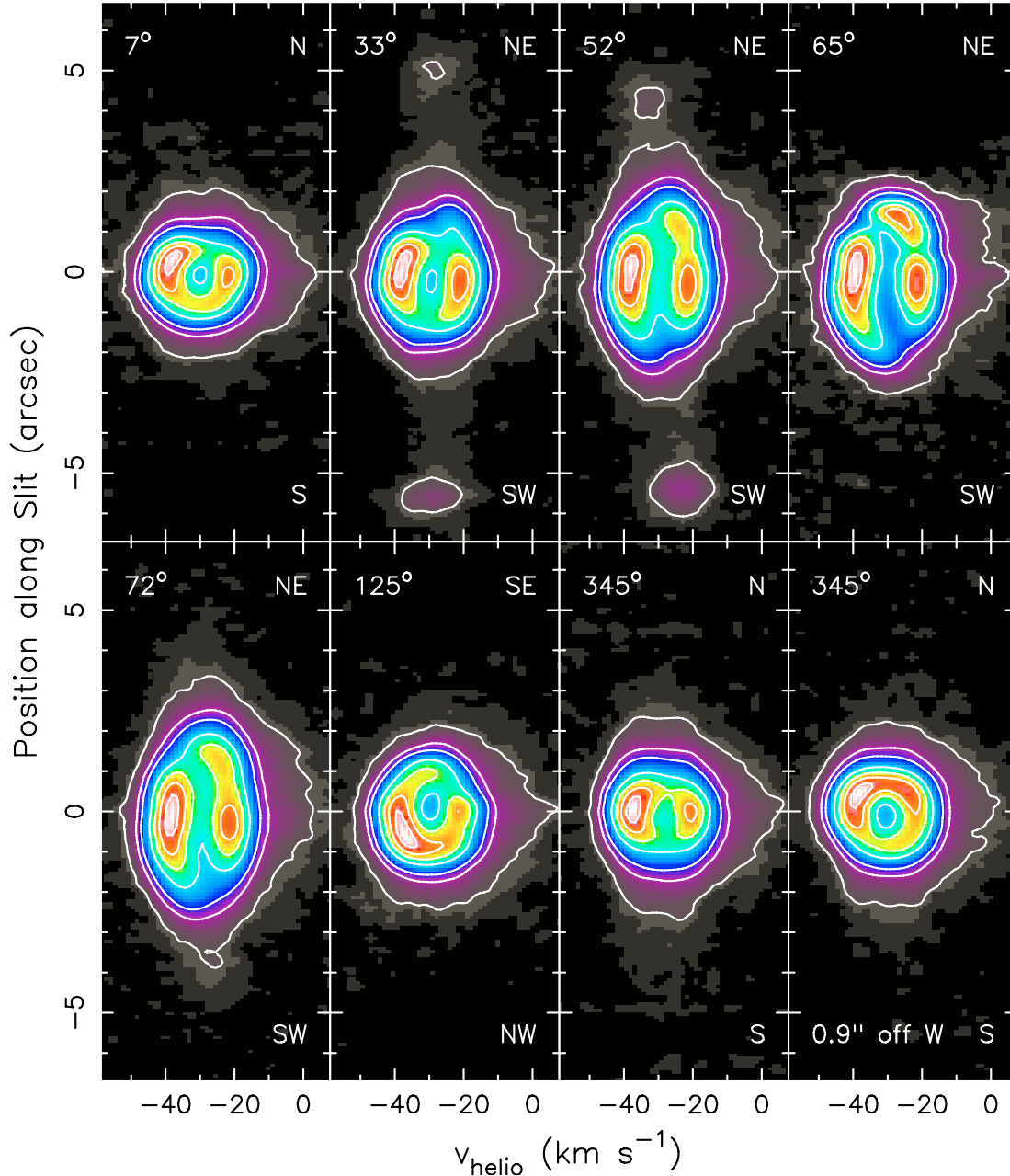


Fig. 2. The position–velocity diagrams of the spectra at H₂ 1–0 S(1). The slit position angles and corresponding spatial directions are indicated at the top and bottom corners. Contours are, from the top to bottom, 90%, 70%, 50%, 30%, 10%, 5%, and 1% of the peak.

2.2. H₂ 1–0 S(1) image

We retrieved the high-resolution H₂ image from the HST archive. IRAS 16594–4656 was observed with *NICMOS* (Malhotra et al. 2002) on-board HST in Cycle 11 (General Observer program 9366, PI: B. Hrivnak) on 12 January 2003. The observations were made with *NICMOS2*, which provides a $19''.2 \times 19''.2$ field of view with $0''.075$ pixel⁻¹ scale, in conjunction with the F212N (H₂) and F215N (H₂ and Br γ continuum) filters. We reduced the data using the standard set of *NICMOS* calibration programs provided in *IRAF/STSDAS* version 3.1¹. A detailed account of the reduction procedure can be found in Ueta et al. (2005). The reduced image is shown in Fig. 1 with the slit positions of the available Phoenix data.

¹ STSDAS is a product of the Space Telescope Science Institute, which is operated by AURA for NASA.

2.3. UVES spectrum

A high resolution echelle spectrum was obtained with *UVES* on the VLT at ESO Paranal in May and June 2000. A detailed account of the observations, reduction procedure, and spectrum can be found in Reyniers (2002).

3. Results

3.1. H₂ 1–0 S(1)

The H₂ 1–0 S(1) position-velocity diagrams in Fig. 2 can be understood in the context of the detailed morphology of H₂ seen in the H₂ *NICMOS* image. The slit positions are shown on the HST H₂ image (Fig. 1). The slit position at 7° primarily goes through the center, which is mostly washed out in the *NICMOS* H₂ image due to the bright central star. The slit position at 65° is

almost along the major axis and going through the bright spot at the tip of the eastern lobe. The slit position at 125° goes through the center at an intermediate angle and captures the bright north-western edge of the lobe.

Reyniers (2002) observed a large spread in radial velocity of the optical lines (from -10 to -40 km s⁻¹) with a small dependence upon excitation potential. The high excitation emission lines seem to have mean radial velocities around -30 km s⁻¹, while the absorption lines have velocities more around -23 km s⁻¹ in the mean. The extracted H₂ profiles are double-peaked. The minimum flux in the H₂ profiles is on average at -29.2 km s⁻¹. Hence the H₂ velocity seems to agree on average with the velocity of the emission lines in the optical spectrum. We adopt -29.2 km s⁻¹ as reference velocity.

The slit position at 7° PA (Fig. 2, top left) shows a toroidal structure of 2''.4 in diameter in the north-south direction at 10% of the peak. The diameter of the shell extends to about 4'' at 1% ($\sim 5\sigma$) of the peak emission. There is little emission around the central star, reinforcing the toroidal appearance. It may correspond to the toroidal equatorial density enhancement (EDE) as seen in the mid-infrared images (Volk et al. 2006). The bulk of the near/approaching side of the shell moves at -38.2 km s⁻¹ and the far/receding side at -21.2 km s⁻¹. Hence, with respect to the reference velocity of -29.2 km s⁻¹, the bulk of H₂ emission appears to expand at about 8 km s⁻¹. This seems low compared to the CO ($J = 2-1$) outflow velocity of 14 km s⁻¹ (Woods et al. 2005). However, the total velocity width, including the wings, is as large as $50.8(\pm 2.2)$ km s⁻¹ at the 1% level. The velocity spread in the wing at the receding side is much larger than at the approaching side.

The slit position at 65° PA (Fig. 2, top right) samples the lobes close to the major axis. In this spectral image the object is most elongated: about 5.5'' at the 1% (2σ) level of the peak. The bulk of the emission is detected within 2'' of the central star, most of it towards the northeast, which corresponds to the main emission region in the HST H₂ image (Fig. 1). The lack of emission at the reference velocity close to the star points to a hollow nature of the shell. At this slit position, the main lobe is separated into two emission regions that are moving away from the central region. The approaching peak is located almost at the center at -39.5 km s⁻¹, while the receding shell is slightly off (0''.3) to the southwest and moves at -20.6 km s⁻¹. The third emission peak represents the northeastern “tip” at 1''.4 from the centre and moves at -26.7 km s⁻¹, which is close to the reference velocity. The approaching peak is strongest and appears to be elongated towards the southwest. The presence of the blob at the northeastern tip seems to make the receding side appear to be elongated towards the northeast, giving a point-symmetric appearance to the whole shell structure.

At 125° PA (Fig. 2, bottom second left) the slit still passes through the EDE, but also through the region of bright H₂ emission in the western lobe. The shell structure appears to be hollow, which is consistent with what is seen in the data at other slit positions. The position-velocity diagram suggests that most of the bright emission at the northwestern side of the lobe comes from the approaching side of the lobe (at 0''.7 to the northwest with a velocity of -36.8 km s⁻¹)

Data at other slit positions have been discussed by Hrivnak et al. (2006). The overall trend of the emission structure is similar for the two data sets at similar position angles, except that the Hrivnak data set covers emission from the clumps located at $\sim 5''$ from the centre. The clumps are almost at the reference velocity. However, especially at the 52° PA, there is a slight velocity difference between these clumps: the clump at the northeast is a bit

blueshifted and the one at the southwest is a bit redshifted compared to the reference velocity. The slit positions at 33° and 125° PA, and as well as at 72° and 345° PA are almost perpendicular to each other. The data confirm the hollow structure which is round and elongated, but the H₂ intensity is not uniformly distributed along the walls.

In general the position-velocity diagrams suggest that (1) the shell is hollow, (2) its axis is nearly aligned with the plane of the sky, (3) the approaching side of the shell shows stronger emission and is elongated towards the southwest, while the position of the emission peak is slightly northeast of the centre, and (4) the receding side of the shell is weaker in emission strength and is elongated towards the northeast, while the position of the emission peak is slightly southwest of the centre. Thus the emission structure appears to be almost point-symmetric in both the spatial and velocity dimensions.

3.2. H₂ 2–1 S(1) emission

Figure 3 shows the H₂ 2–1 S(1) position-velocity diagrams (left column) and H₂ 2–1 S(1) contours overlaid on the H₂ 1–0 S(1) position-velocity diagrams (right column) at 7°, 65°, and 125° PA, from top to bottom, respectively). The H₂ 2–1 S(1) and 1–0 S(1) emission seem to be extended in a similar manner, except that (1) H₂ 2–1 S(1) seems to originate a bit closer to the central star than H₂ 1–0 S(1) and (2) H₂ 2–1 S(1) does not show an elongation towards the northeast (in the receding lobe) and to the southwest (in the approaching lobe) at 65° PA. Also, H₂ 2–1 S(1) does not seem to show the large velocity dispersion towards the red as in the H₂ 1–0 S(1) images. The lowest contour (at 1% of the peak) displays elongations into higher/lower velocities near the centre, but this is probably residual continuum emission that has not been completely removed.

3.3. [Fe II] 1.645 μm emission

Figure 4 shows the [Fe II] position-velocity diagrams (left column) and the [Fe II] contours overlaid on the H₂ 1–0 S(1) position-velocity diagrams (right column) at 7°, 65°, and 125° PA, from top to bottom, respectively. From the contour-overlaid images it is clear that the H₂ and [Fe II] emission originates from different regions.

The seeing of the night was between 0''.7 and 0''.9 in the R-band. Using the stellar continuum we measure a seeing of 0''.8, 0''.7, and 0''.6 on average at 7°, 65°, and 125° respectively. The Gaussian *FWHM* of the [Fe II] profile is 0''.98, 1''.05, and 0''.94 at 7°, 65°, and 125° respectively. Hence we conclude that the [Fe II] emission region is extended. At an assumed luminosity of $10^4 L_{\odot}$ and distance of 2.2 kpc (Paper I) the deconvolved Gaussian *FWHM* diameter of the emitting region would be 0.004 pc \pm 0.001 pc (or 80 ± 20 AU). Assuming a stellar temperature of 14 000 K (Reyniers 2002), this is about 1800 stellar radii.

The extracted profile at 7° PA is shown in Fig. 5. The [Fe II] emission peaks at the reference velocity of -29.2 km s⁻¹ and the Gaussian *FWHM* of the profiles are 31.8 km s⁻¹, 33.1 km s⁻¹, and 33.1 km s⁻¹ at 7°, 65°, and 125° PA, respectively. The total width of the profile at 1% of the peak is 62 km s⁻¹. The [Fe II] emission appears to come from the inner region, close to the star at all position angles and shows a larger velocity dispersion than the H₂ emission.

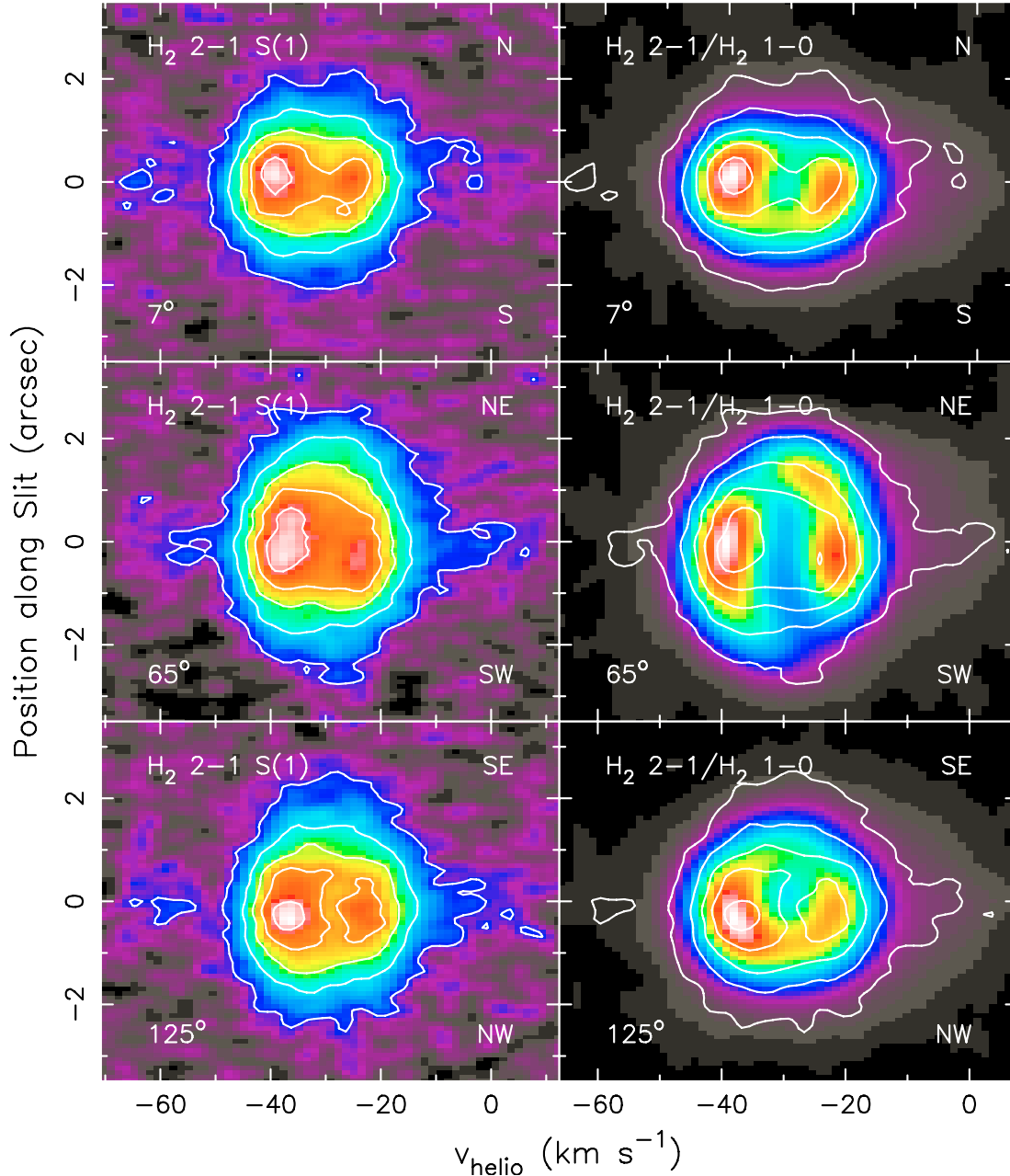


Fig. 3. The position–velocity diagrams of the spectra at H₂ 2–1 S(1) (left) and H₂ 2–1 S(1) contours overlaid on the H₂ 1–0 S(1) images (right). The slit position angles and corresponding spatial directions are indicated at the top and bottom corners. Contours are, from the top to bottom, 90%, 70%, 50%, 30%, and 10% of the peak. When contours are overlaid, the H₂ 1–0 S(1) images are smoothed to have matching spatial and spectral resolution.

3.4. Pa β and other Paschen lines

One useful image of Pa β was obtained at 7° PA before the dome had to be closed due to bad weather. The Pa β emission is centered on the star. The seeing was at least 1''.5, much worse than for the [Fe II] observations, and the spatial profile remained unresolved.

In Fig. 6 we compare Pa β with the [Fe II] profile at 7° PA. The peak of the Pa β profile is at -21 km s^{-1} , while the peak of [Fe II] is at -29.8 km s^{-1} . The velocity of the peak of the Pa β profile is closer to the average velocity of the absorption lines in the optical spectrum, while the velocity of the peak of the [Fe II] emission is closer to the velocity of the optical emission lines. Pa β is faint, but the normalized profile is considerably broader than the [Fe II] emission profiles. The Gaussian

FWHM is 48.2 km s^{-1} and the total profile width at 1% of the peak is $\sim 75 \text{ km s}^{-1}$. The peak of the profile appears to be asymmetric. In Fig. 6 we compare the Pa β profile with two other Paschen lines (Pa δ at 1004.9373 nm and Pa $_{20}$ at 839.2396 nm) from the UVES spectrum. The absorption profile of Pa 3–20 has very broad wings and some emission. This emission becomes stronger for lower members of the Paschen series.

3.5. Optical [O I] and [C I] emission lines

The only forbidden emission lines in the optical, UVES spectrum (Reyniers 2002) are the [O I] lines at 5577.3387 , 6300.304 , 6363.777 \AA and the [C I] lines at 8727.12 , 9824.13 , and 9850.26 \AA . We have plotted the strongest line of each element

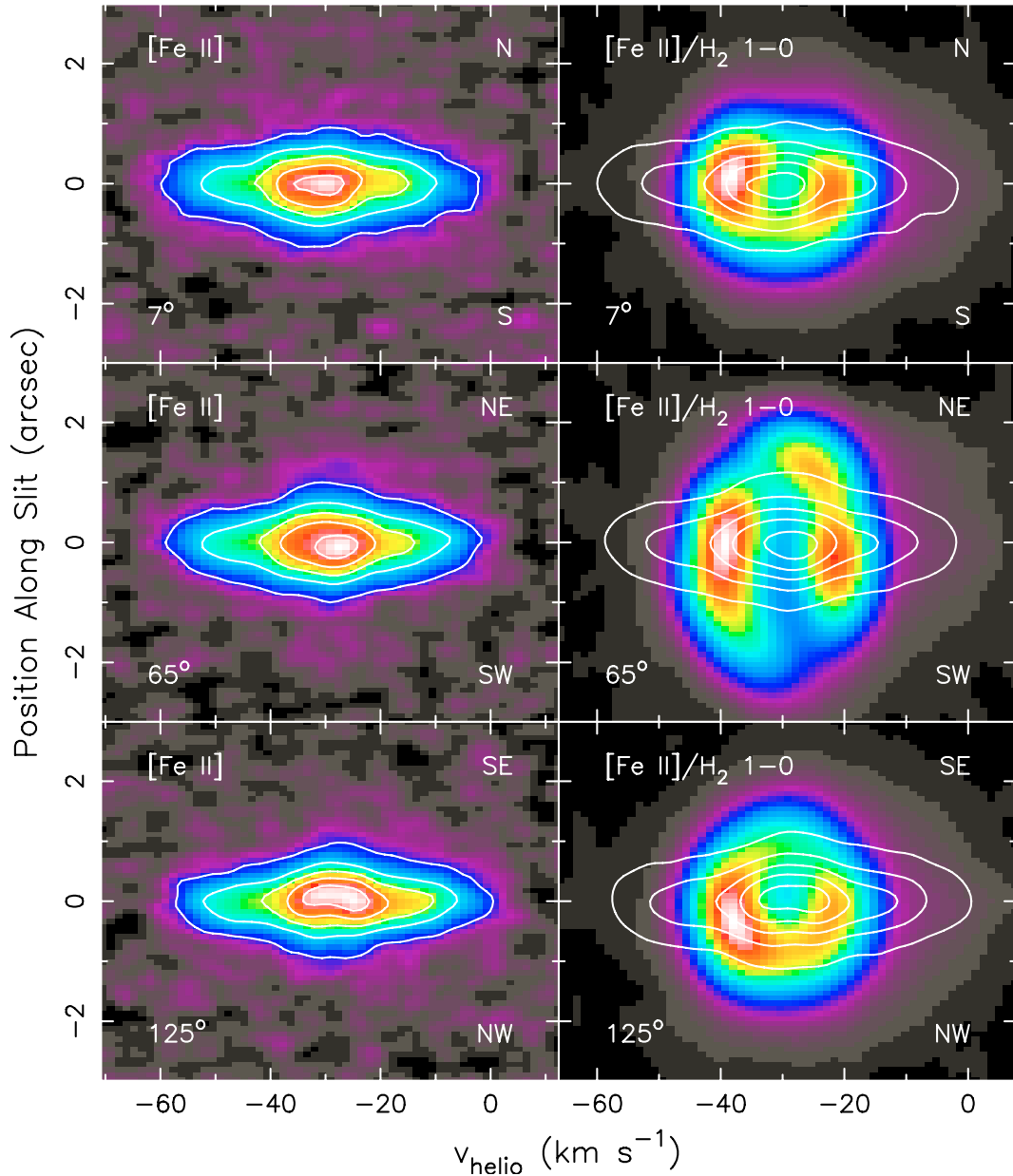


Fig. 4. [Fe II] color images with [Fe II] contours overplotted (*left*) and [Fe II] contours overplotted on the H₂ 1–0 S(1) images (*right*) at 7°, 65°, and 125° PA from top to bottom, respectively.

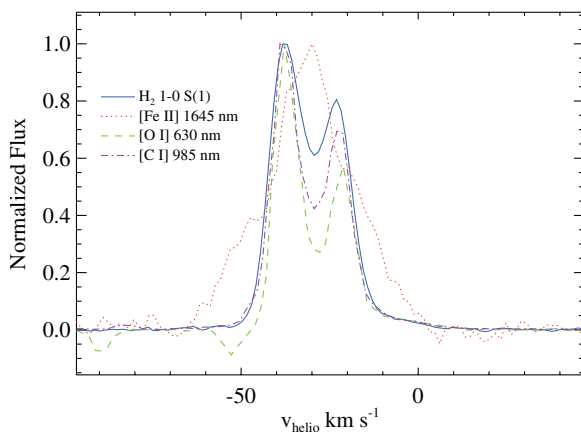


Fig. 5. Velocity profiles of the extracted spectra of H₂ 1–0 S(1) at 7° PA, [Fe II] at 7° PA, [O I], and [C I]. Each line is continuum subtracted and normalized to the peak intensity.

in Fig. 5. We notice that the optical [O I] and [C I] emission lines have a profile very similar to the H₂ emission line. Because the UVES spectra were obtained with the image slicer, we have no spatial information. However based on their similar profiles, they seem to originate in the shock which produces the H₂ emission. In PNe, collisionally excited C⁰ has also been observed to coexist mainly with H₂, making it an invaluable probe of H₂ emitting regions (Liu et al. 1995). In old extended PNe, such as the Ring nebula, the [O I] 6300 Å line is also found to largely follow the near-infrared H₂ emission (Liu & Barlow 1996).

The [C I] λ 9824, 9850 Å lines decay from the same upper level, so their intensity ratio depends only on the relative transition probabilities, and is purely determined by atomic parameters. Similarly, the [O I] λ 6300, 6363 Å line ratio is also purely determined by atomic parameters. In the case of collisional excitation, the observed [C I] line ratio $(I_{9824} + I_{9850}) / I_{8727}$ and the [O I] ratio $(I_{6300} + I_{6363}) / I_{5577}$ provide each a

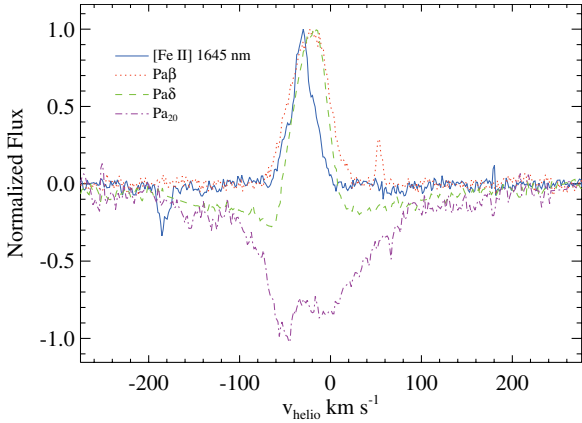


Fig. 6. Velocity profiles of the extracted spectra of 3 Paschen lines and [Fe II]. Each line is continuum subtracted and normalized to the peak intensity.

direct diagnostic of the electron temperature, assuming the electron density is known. Using the extinction derived in Paper I ($R_V = 4.2$, $E(B - V) = 1.78$), we corrected the lines for extinction and calculated both ratios. For the [C I] line ratio we obtain a value of 1.5 ± 0.5 . For the [O I] ratio we obtain a value of 6.0 ± 1.0 . The UVES slit width was $0''.7$, orientated east-west, and, because of the use of the slicer, no atmospheric dispersion correction could be applied. The shift between the 5577 \AA and the 6363 \AA lines is $0''.2$. Because the object is extended, this probably has little effect on the ratio. We checked whether the [C I] lines are affected by telluric absorption using the transition probabilities calculated by Nussbaumer & Rusca (1979). The I_{9824} / I_{9850} theoretical line ratio is 0.338 and our value is within 3% of this theoretical value. Hence in our spectra these lines are not affected by telluric absorption.

In order to calculate the electron temperature from the [O I] or [C I] line ratios, we need to assume an electron density. Usually, the [N I] doublet ratio $\lambda 5200.42 / 5197.95 \text{ \AA}$ is one of the very few density-sensitive diagnostics observable from neutral species in the optical region. It is a good tracer of the electron density in regions where [C I] and [O I] are observed. However the [N I] lines are not detected. This is not due to ionization of nitrogen. The ionization potential of N^0 (14.534 eV) is a bit larger than that of H^0 (13.62 eV) and O^0 (13.60 eV), and no [O II] or [N II] lines are observed in the optical spectrum. Nitrogen doesn't seem to be underabundant (Reyniers 2002) either. Hence the absence of the [N I] lines indicates that the [N I] lines are collisionally de-excited in the high-density region where the [C I] and [O I] lines originate. This is due to the relatively low critical densities of the [N I] lines: about 4830 and 1160 cm^{-3} at $T_e = 10000 \text{ K}$ for the upper levels of the $\lambda 5198$ and 5200 \AA lines, respectively (Zeippen 1982; Berrington & Burke 1981).

For carbon, the critical densities of the $2p^2 \text{ } ^1D_2$ level from which the $\lambda 9824 \text{ \AA}$ and 9850 \AA transitions originate are 4.8×10^4 , 2.2×10^4 , and $1.6 \times 10^4 \text{ cm}^{-3}$ for $T_e = 1000, 5000,$ and 10000 K , respectively (Liu et al. 1995) and $1.1 \times 10^7 \text{ cm}^{-3}$ for the 1S_0 level from which the $\lambda 8727 \text{ \AA}$ line originates (Mendoza 1983; Berrington & Burke 1981). Hence the low value derived from the [C I] ratio indicates that the 1D_2 level population is quenched by electron impacts, and that the electron density in the shocked region would be higher than 10^5 cm^{-3} . The critical density for the 1D_2 level from which the $\lambda 6300 \text{ \AA}$ and 6363 \AA lines originate is $1.9 \times 10^6 \text{ cm}^{-3}$ at 10000 K and is $1.1 \times 10^8 \text{ cm}^{-3}$ for the 1S_0 level from which the $\lambda 5577 \text{ \AA}$ line

originates (Mendoza 1983; Berrington & Burke 1981). The [O I] line ratio is insensitive to electron densities below approximately 10^6 cm^{-3} at 10000 K .

As we have no constraint on the electron density, we have used the photo-ionization code Cloudy (version 07.10.15) last described by Ferland (1998) to calculate a grid of [O I] and [C I] line ratios in function of T_e and n_e . The detection of strong collisionally excited [C I] and [O I] line emission, but no [O II] line emission, requires that there must be a region which is predominantly neutral, but hot enough for effective excitation of the levels in [O I], which implies $6000 \lesssim T_e (\text{K}) \lesssim 10000$. The electron density must be higher than 10^4 cm^{-3} for the [N I] lines to be collisionally de-excited. We considered $3.7 \lesssim \log(T_e/\text{K}) \lesssim 4.0$ and $4.0 \lesssim \log(n_e/\text{cm}^{-3}) \lesssim 8.0$, using steps of 0.1 dex and 0.25 dex respectively. The [O I] ratio corresponds to electron densities of 3×10^6 to $5 \times 10^7 \text{ cm}^{-3}$ for electron temperatures of 10000 K to 6000 K , respectively. At these electron temperatures the electron densities derived from the [C I] line ratio are 10^5 – $3 \times 10^5 \text{ cm}^{-3}$.

In summary: There is no indication of ionized gas in the optical spectrum of IRAS 16594-4656. The forbidden [O I] and [C I] emission are collisionally excited and originate in a very high density region ($3 \times 10^6 \lesssim n_e \lesssim 5 \times 10^7 \text{ cm}^{-3}$), in the same shock which produces the H₂ emission.

4. Discussion

4.1. Kinematics and morphology of the H₂ 1–0 S(1) emission.

In order to investigate the 3-dimensional structure of the lobes, we constructed a data cube using all existing data in H₂ 1–0 S(1). First we rectified the H₂ 1–0 S(1) data at each position angle to have a pixel scale of $0.085'' \text{ pix}^{-1}$ in the spatial dimension and of 1.263 km s^{-1} in the velocity dimension. Then we aligned the position–velocity frames using the location of the continuum peak in the spatial dimension and the reference velocity in the velocity dimension. Next we spline-interpolated the surface brightness as a function of position angle in each pixel in the position velocity frame based on the original seven frames. Finally we projected the interpolated 3-dimensional data onto a 3-dimensional Cartesian grid.

Figure 7 shows the velocity channel maps that are recovered from the reconstructed data cube in H₂ 1–0 S(1). Each channel has a width of 5.05 km s^{-1} . Maps near the reference velocity indicate that the H₂ emission is strong in both lobes, but stronger in the western lobe than in the eastern lobe, which is also seen in the total intensity map in Fig. 1. They also indicate that there is in fact less emission along the waist region of the shell. This can also be seen from the position velocity maps at 7° and 345° , but the velocity channel maps depict it more eloquently. Thus, the overall 3-dimensional structure of the shell is such that the majority of the H₂ emission is distributed as hollow bipolar lobes, one at the approaching side and one at the receding side of the shell. The approaching side of the shell is elongated towards the west while the receding side of the shell is elongated towards the east.

Assuming a homologous expansion, *i.e.*, an expansion with $v \propto r$, the velocity axis in the recovered data cube corresponds to a spatial axis along the line of sight. This allows us to visualize the 3-dimensional structure of the spatial distribution of H₂. Figure 8 shows the 3-dimensional representation of the central shell of IRAS 16594-4656, for which the surface contour has been constructed based on the reconstructed data cube at 30% of

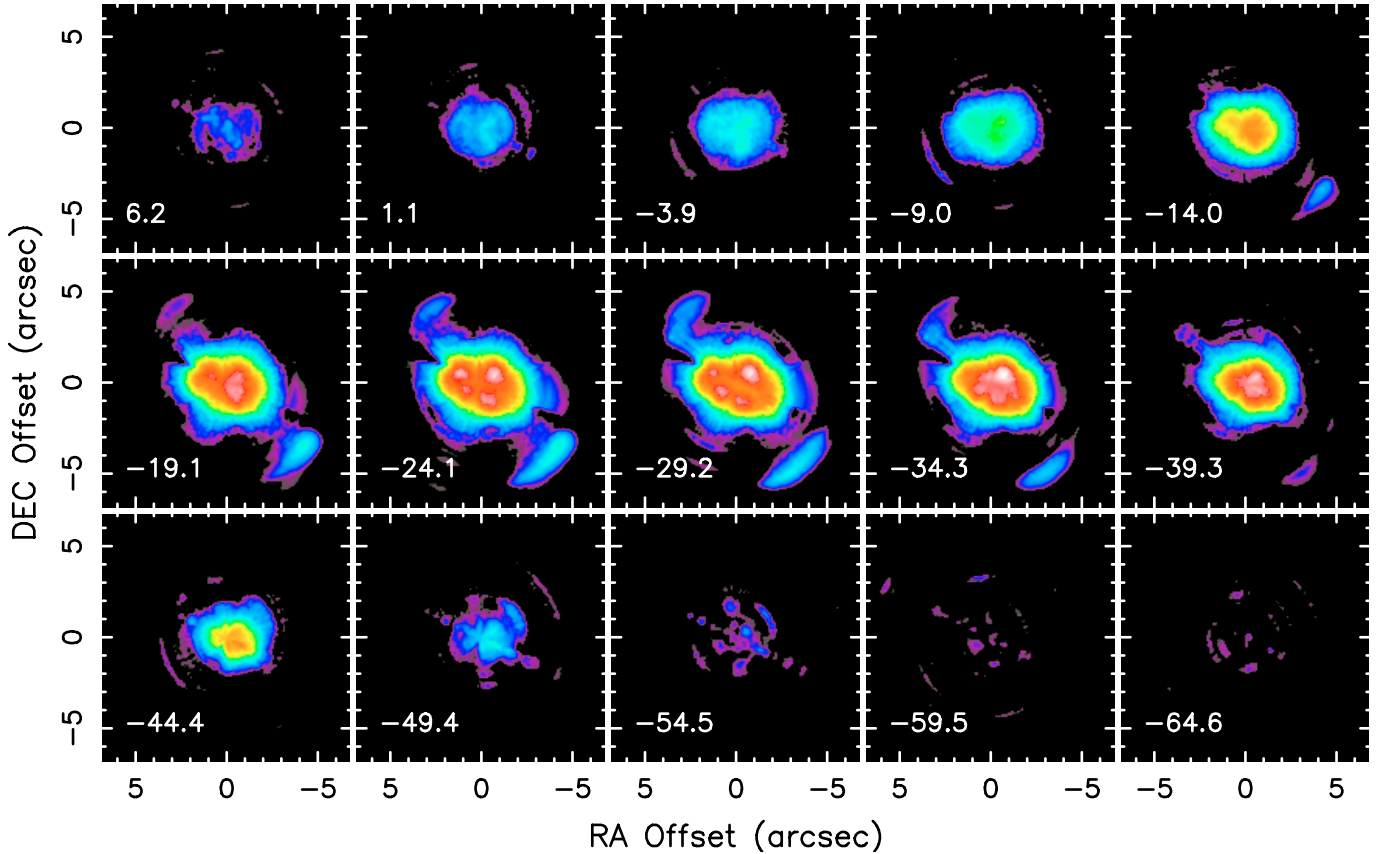


Fig. 7. The velocity channel maps of the reconstructed H₂ 1–0 S(1) data cube centered around the reference velocity of -29.2 km s^{-1} . Each channel has a width of 5.05 km s^{-1} and its central velocity is indicated at the bottom left corner in km s^{-1} .

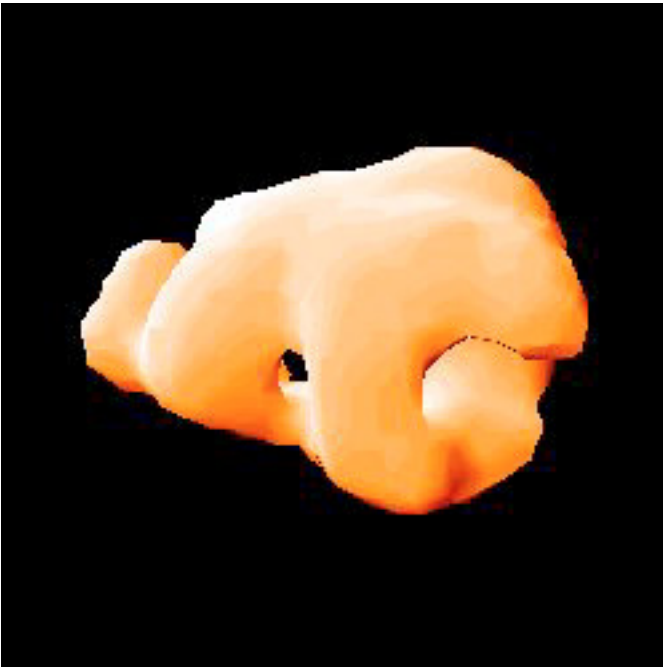


Fig. 8. 3-dimensional rendition of the shell structure of IRAS 16594–4656. The surface represents an isointensity contour at roughly 30% of the peak intensity.

the peak emission. Figure 8 shows the bottom right view of the surface contour, illuminated obliquely from the southwest side by a fiducial light source. The 3-dimensional volume shows the central cavity and the hollowness of the shell along the polar axis

of the bipolar lobes, the western and eastern elongations in the approaching and receding sides of the shell, and the holes on the surface at the top and bottom of the equatorial regions.

4.2. Shock properties

In Paper I we concluded that the H₂ emission in IRAS 16594–4656 is mainly collisionally excited and that (1) the line ratios indicate that the H₂ emission originates in a 20 to 30 km s^{-1} C-type shock in 10^3 cm^{-3} material (Le Bourlot et al. 2002), (2) we postulated that the C-shocks occur where the fast wind is funneled through the EDE, which may harbor a magnetic field, but we noted that the H₂ emission could also be present in the lobes, excited by shocks caused by a molecular outflow impinging on the AGB envelope, and (3) we noted that in principle H₂ and Fe⁺ cannot coexist in the same shocked region in substantial quantities.

In previous sections we showed that the H₂ emission is indeed present at the edge of the EDE, but is more intense at the edge of the lobes. The H₂ emission appears to be excited in shocks between the AGB ejecta and the post-AGB wind.

In this paper we found that the [O I] and [C I] emission lines are very similar to the H₂ profiles in shape and velocity. They may originate in the shock close to where the H₂ emission originates. Their line ratios indicate a very high density of 3×10^6 to $5 \times 10^7 \text{ cm}^{-3}$ in the shock. At this high density the rotational temperature of $1440 \pm 80 \text{ K}$ derived in Paper I corresponds to a 10 to 20 km s^{-1} C-type shock into 10^6 to 10^7 cm^{-3} material (Le Bourlot et al. 2002). However at such high densities, the ionization of the metals may suffice to produce a J-type shock (Smith 1994). If this were the case, the rotational temperature

determined in Paper I and the high density would also be consistent with a J-type shock of 5 to 10 km s⁻¹ into 10⁵ to 10⁶ cm⁻³ material (Wilgenbus et al. 2000). At these low velocities and high densities the J-type shock will not dissociate H₂, and the H₂ emission will remain strong.

[Fe II] 1.64 μm is a cooling line of gas that is excited predominantly by shocks. It is a very good tracer of gas shocked by energetic events in the absence of photoionization, which is the case for IRAS 16594-4656. [Fe II] emission cannot be excited in the presence of C-shocks alone, as C-type shocks do not produce emission from ionized species such as Fe⁺. [Fe II] emission is well modelled by fast dissociative J-type shocks. In slow non-dissociative J-shocks, the [Fe II] emission drops rapidly with the shock velocity (Gredel 1994). Hence [Fe II] emission arises from fast dissociating and ionizing shocks, while the H₂ emission arises from locations where the shock velocities are low enough, not to cause destruction of H₂. We see indeed that the H₂ and [Fe II] emission line profiles and spatial extent are sufficiently different to confirm that they mainly come from different regions. The [Fe II] emission appears to originate in a region close to the central star within the hollow structure outlined by the H₂ emission. The [Fe II] emission is not located along the side walls of the hourglass, as was considered as one of the possibilities in Paper I and is the case in Hubble 12. Neither is it present as blobs in discrete shock fronts in the lobes as is the case for M 1-92 (Davis et al. 2005). The [Fe II] emission may be due to shocks in the stellar wind or originate in a circumstellar or circumbinary disk.

5. Conclusions

The H₂ emission is excited in slow 5 to 20 km s⁻¹ shocks into dense material at the edge of the lobes, caused by the interaction of the AGB ejecta and the post-AGB wind. The 3D representation of the H₂ emission shows a hollow structure. There is less H₂ emission in the equatorial region. The collisionally excited [O I] and [C I] optical emission lines have a similar profile compared to the extracted H₂ profile and appear to be produced in the same shock. They all indicate an expansion velocity of ~8 km s⁻¹ and the presence of a neutral, very high density region of about 3 × 10⁶ to 5 × 10⁷ cm⁻³. The [Fe II] emission is not present in the lobes, but originates close to the central star. It originates in fast shocks in the post-AGB wind, or in a circumstellar or circumbinary disk. The Paβ emission also appears to originate close to the star. The total width of the [Fe II] and Paβ emission line profiles is 62 and 75 km s⁻¹ respectively, at 1% of the peak.

Acknowledgements. TU and PvH acknowledge support from the Belgian Science Policy Office in the framework of the IUAP5/36 project. PvH acknowledges support from the Belgian Science Policy Office through grant MO/33/017. MR acknowledge financial support from the Fund for Scientific Research – Flanders (Belgium). We thank B. Hrivnak for stimulating discussions.

References

- Arrieta, A. Torres-Peimbert, S. 2003, ApJS, 147, 97
 Balick, B., & Frank, A. 2002, ARA&A, 40, 493
 Berrington, K. A., & Burke, P. G. 1981, Planet. Space Sci., 29, 377
 Cardelli, J. A., Clayton, G. C., & Mathis, J. S. 1989, ApJ, 345, 245
 Davis, C. J., Smith, M. D., Gledhill, T. M., & Varricatt, W. P. 2005, MNRAS, 360, 104
 Ferland, G. J., Korista, K. T., Verner, D. A., et al., PASP, 110, 761
 Dickinson, M., et al. 2002, in HST NICMOS Data Handbook Version 5.0, ed. B. Mobasher (Baltimore: STScI)
 García-Hernández, D. A., Manchado, A., García-Lario, et al. 2004, in Asymmetrical Planetary Nebulae III, ed. M. Meixner, J. Kastner, B. Balick, & N. Soker (San Francisco: ASP), ASP Conf. Ser., 313, 367
 García-Lario, P., Manchado, A., Ulla, A. L., & Manteiga, M. 1999, ApJ, 513, 941
 Gredel, R. 1994, A&A, 292, 580
 Hinkle, K. H., Blum, R., Joyce, R. R., et al. 2002, Proc. SPIE, 4834, 353
 Hrivnak, B. J., Kwok, S., & Su, K. Y. L. 1999, ApJ, 524, 849
 Hrivnak, B. J., Kwok, S., & Su, K. Y. L. 2001, AJ, 121, 2775
 Hrivnak, B. J., Kelly, D. M., Su, K. Y. L., Kwok, S., & Sahai, R. 2005, ApJ, 650, 237
 Hrivnak, B. J., Smith, N., Su, K. Y. L., et al. 2006, in Planetary Nebulae in our Galaxy and Beyond, ed. M. J. Barlow, & R. H. Méndez, IAU Symp., 234, 423
 Kastner, J. H., Weintraub, D. A., Gatley, I., Merrill, K. M., & Probst, R. G. 1996, ApJ, 462, 777
 Kelly, D. M., & Hrivnak, B. J. 2005, ApJ, 629, 1040
 Kwok, S. 1993, ARA&A, 31, 63
 Le Bourlot, J., Pineau des Forets, G., Flower, D. R., & Cabrit, S. 2002, MNRAS, 332, 985
 Liu, X.-W., & Barlow, M. J. 1996, MNRAS, 279, 511
 Liu, X.-W., Barlow, M. J., Danziger, I. J., & Clegg, R. E. S. 1995, MNRAS, 273, 47
 Mendoza, C. 1983, IAU Planetary nebulae (Dordrecht: D. Reidel Publishing Co.), 103, 143
 Malhotra, S., et al. 2002, NICMOS Instrument Handbook, Version 5.0 (Baltimore: STScI)
 Nussbaumer, H., & Rusca, C. 1979, A&A, 72, 129
 Nussbaumer, H., Schmid, H. M., & Vogel, M. 1989, A&A, 211, L27
 Reyniers, M. 2002, PhD Thesis, K.U. Leuven
 Rothman, L. S., Barbe, A., Chris Benner, D., et al. 2003, J. Quant. Spectr. Radiat. Trans., 82, 5
 Sánchez Contreras, C., Bujarrabal, V., Castro-Carrizo, A., Alcolea, J., & Sargent, A. 2004, ApJ, 617, 1142
 Smith, M. D. 1994, MNRAS, 266, 238
 Smith, N., & Gehrz, R. D. 2005, AJ, 129, 969
 Su, K. Y. L., Kwok, S., & Hrivnak, B. J. 2000, Am. Astron. Soc. Meet. 197, 131.03
 Su, K. Y. L., Hrivnak, B. J., & Kwok, S. 2001, AJ, 122, 1525
 Ueta, T., & Meixner, M. 2003, ApJ, 586, 1338
 Ueta, T., Murakawa, K., & Meixner, M. 2005, AJ, 129, 1625
 Ueta, T., Murakawa, K., & Meixner, M. 2007, AJ, 133, 1345
 Van de Steene, G. C., & Pottasch, S. R. 1993, A&A, 274, 895
 Van de Steene, G. C., & van Hoof, P. A. M. 2003, A&A, 406, 773
 Van de Steene, G. C., van Hoof, P. A. M., & Wood, P. R. 2000a, A&A, 362, 984
 Van de Steene, G. C., Wood, P. R., & van Hoof, P. A. M. 2000b, in Asymmetrical Planetary Nebulae II: From Origins to Microstructures, ed. J. H. Kastner, N. Soker, & S. Rappaport, ASP Conf. Ser., 199, 191
 Volk, K., Hrivnak, B. J., Su, K. Y. L., & Kwok, S. 2006, ApJ, 651, 294
 Weintraub, D. A., Huard, T., Kastner, J. H., & Gatley, I. 1998, ApJ, 509, 728
 Wilgenbus, D., Cabrit, S., Pineau des Forets, G., & Flower, D. 2000, A&A, 356, 1010
 Woods, P. M., Nyman, L.-A., Schöier, F. L., et al. 2005, A&A, 429, 977
 Zeippen, C.J. 1982, MNRAS, 198, 111